Error and Uncertainty Degrade Topographic Corrections of Remotely Sensed Data

Jeff Dozier[1], Edward H. Bair[2], Latha Baskaran[3], Philip G. Brodrick[3], Nimrod Carmon[3], Raymond F. Kokaly[4], Charles E. Miller[3], Kimberley R. Miner[3], Thomas H. Painter[5], and David R. Thompson[3]

[1]Bren School of Environmental Science & Management, University of California, Santa Barbara, CA 93106. [2]Earth Research Institute, University of California, Santa Barbara, CA 93106. [3]Jet Propulsion Laboratory, California Institute of Technology, Pasadena, CA 91109. [4]U.S. Geological Survey, Lakewood, CO 80225. [5]Joint Institute for Regional Earth System Science and Engineering, University of California, Los Angeles, CA 90095.

Corresponding author: Jeff Dozier (dozier@ucsb.edu)

Key Points:

- Mountain topography causes apparent remotely sensed reflectance to differ from the intrinsic reflectance of the surface.
- Errors in illumination geometry derived from globally available digital elevation models introduce substantial uncertainty into analyses.
- Retrieval of the intrinsic reflectance and thereby surface properties requires correction for topographic illumination geometry.

Abstract

Chemical and biological composition of surface materials and physical structure and arrangement of those materials determine the *intrinsic* spectral reflectance of Earth's land surface at the plot scale. As measured by a spaceborne or airborne sensor, the *apparent* reflectance depends on the intrinsic reflectance, the surface texture, the contribution and attenuation by the atmosphere, and the topography. Compensation or correction for the topographic effect requires information in digital elevation models (DEMs). Available DEMs with global coverage at ~30 m spatial resolution are derived from interferometric radar and stereo-photogrammetry. Locally or regionally, airborne lidar altimetry, airborne interferometric radar, or stereo-photogrammetry from airborne or fine-resolution satellite imagery produces DEMs with finer spatial resolutions. Characterization of the quality of DEMs typically expresses the root-mean-square (RMS) error of the elevation, but the accuracy of remote sensing retrievals is acutely sensitive to uncertainties in the topographic properties that affect the illumination geometry. The essential variables are the cosine of the local illumination angle and the shadows cast by neighboring terrain. We show that calculations with globally available DEMs underrepresent shadows and consistently underestimate the values of the cosine of illumination angle; the RMS error increases with solar zenith angle and in more rugged terrain. Analyzing imagery of Earth's mountains from current and future missions requires addressing the uncertainty introduced by errors in DEMs on algorithms that estimate surface properties from retrievals of the apparent spectral reflectance. Intriguing potential improvements lie in novel methods to gain information about topography from the imagery itself.

Plain Language Summary

Digital Elevation Models (DEMs) are used across scientific disciplines to understand the topography of Earth's surface. Small errors in the estimates of elevation lead to larger errors in calculations of the solar illumination on the terrain and portions that are in shadow, thereby leading to misinterpretation of remotely sensed imagery from airplanes and satellites. Here, we present estimates of the errors and uncertainty in DEM retrievals, and we identify some outright mistakes. Compensating for uncertainty will help upcoming satellite missions to develop algorithms that consider the effect of Earth's topography, improving the characterization of remotely sensed attributes of the planet's surface.

1 Introduction

We use remotely sensed data to derive geophysical and biological properties of importance to the study of Earth and other planets. On Earth these analyses must include mountains, which play a key role in the planet's climate, hydrology, ecology, and geology. For example, mountains drive orographic enhancement of precipitation and lead to their function as the world's water towers, resources at risk in a warming climate (Immerzeel et al., 2020; Viviroli et al., 2007). About a quarter of Earth's land surface is mountainous, but mountain snowmelt supplies water resources for more than one billion people (Mankin et al., 2015), serving an important water storage role as climate warming transitions some snow to rain (Barros, 2013).

Further, vegetation changes in high mountains indicate carbon-dioxide fertilization in areas where the partial pressure of all gases is lower (Shugart et al., 2001). Combinations of drought and fire affect mountain forests and sources of water (Moody & Martin, 2001). The critical role that mountains serve as water towers and vegetation hotspots may change under climate change, contributing to hazards to people living in or relying on mountain resources (Kirschbaum et al., 2020). The recent National Academies' Decadal Survey for Earth science and applications, *Thriving on our Changing Planet,* reflects these multiple concerns, with some recommendations calling for observations "at topographic scale" to reflect the diversity of hydrologic and vegetation dynamics across elevations (National Academies of Sciences, Engineering, & Medicine, 2018).

Analysis of the topographic effect requires information in digital elevation models of the bare surface, usually but not universally meaning DEMs, as distinct from digital surface models (DSMs) that include vegetation, buildings, or other features. We consider two globally available DEM datasets: the NASADEM (Buckley, 2020) and the Copernicus DEM (European Space Agency, 2021), both distributed at a resolution of 1 arcsec (~30 m at the Equator). Locally or regionally, finer-resolution DEMs are available, so we consider three of those, which were derived by lidar, interferometric synthetic aperture radar, and structure-from-motion stereo photogrammetry from images from commercial satellites. Our analysis considers the fine-resolution DEMs, in three different terrains, to provide the best assessment of the topographic effects on illumination geometry, and we compare those assessments to those derived from the two globally available datasets.

Characterization of the quality of DEMs typically assesses the vertical accuracy of the elevation. Uuemaa et al. (2020) compared globally available products with fine-resolution lidar elevations; they estimated root-mean-square (RMS) errors at 8-10 m for the NASADEM and TanDEM-X, the primary source of data for the Copernicus DEM. Guth and Geoffroy (2021) compared several datasets with airborne lidar and ICESat-2 data and preferred the Copernicus DEM based on its ability to penetrate vegetation canopies and retrieve bare-Earth elevations.

However, the focus on elevation errors misses the effect of the topography on remotely sensed information, which lies with the illumination geometry. The cosine of the local illumination angle and the shadows cast by neighboring terrain are the most important variables. We therefore assess the DEMs based on their ability to provide insight into the relationship between intrinsic and apparent spectral reflectance and thereby enable retrieval of properties of the surface important to the study of Earth science, such as snow albedo (Bair et al., 2021; Painter et al., 2013) and ecosystem composition (Bogan et al., 2019).

2 An Illustration of the Problem

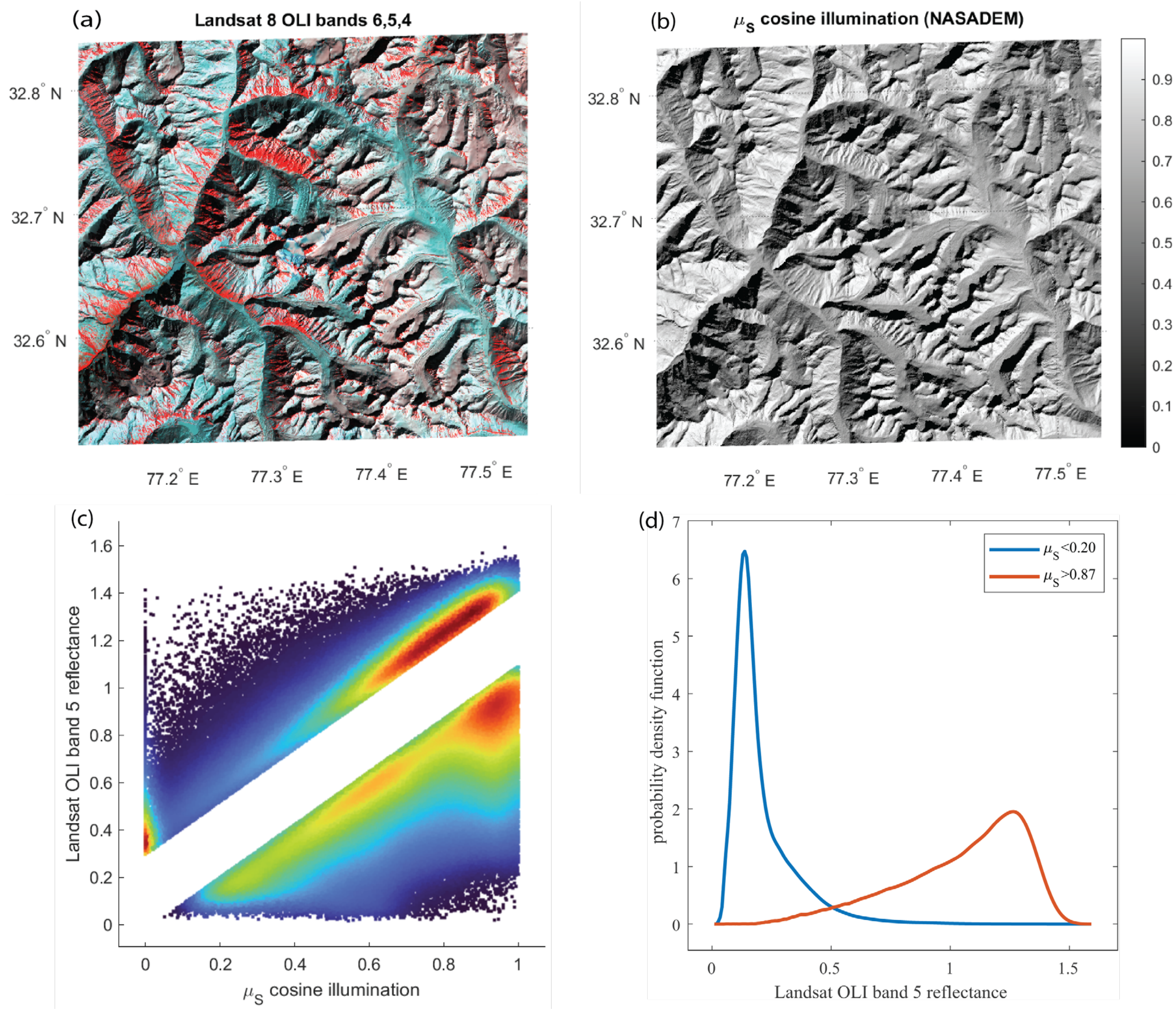

Figure 1. Upper left image (a) shows a portion of a Landsat 8 OLI image in the Indian Himalaya from 22 February 2016 at UTC 05:24. Upper right image (b) shows the illumination at the same time over a NASADEM matching the Landsat image. Lower left scatter density diagram (c) shows the Landsat band 5 top-of-atmosphere reflectance ($\pi \times$ radiance/irradiance) on the vertical axis and the cosine of illumination on the horizontal axis. The colors show density of points, with red and yellow indicating high concentrations values. The blank area eliminates the values within 1 RMSE of the linear regression $f(x) = ax + b$. Clearly problematic are the values in the upper left corner, showing high reflectance values in terrain that the DEM shows to be shaded or obliquely illuminated. The lower right graph (d) shows probability density functions of the reflectance values in two illumination categories, $\mu_S < 0.2$ and $\mu_S > 0.87$, covering the same fractions of the image's values. Each pdf has a long tail. Those in the tail of the low illumination category indicate that the illumination cosine is not correctly estimated and is too small. With a correct DEM, we would not see such high reflectance values at low illumination angles.

Figure 1 shows two images and two graphs. The upper row shows a portion of a Landsat 8 OLI image of the Indian Himalaya, acquired on 22 February 2016 over the Himachal Pradesh state of India. The other image in the upper row shows a calculation of the cosine of the solar illumination angle at the same date and time as the Landsat image, using elevation data from NASADEM (Buckley, 2020). Superficially, they appear to match, the bright areas in the Landsat image corresponding to the highly illuminated pixels. However, the scatter density plot in the lower row, with cosine of illumination on the horizontal axis and top-of-atmosphere reflectance ($\pi \times$ radiance/irradiance) in Landsat OLI band 5 (851-879 nm) on the vertical axis, indicates some problematic values. We chose band 5 because of the small fraction of diffuse illumination in the solar spectrum in those wavelengths. The high reflectance values in the upper left corner of the scatter plot correspond to pixels either in the shadow or with highly oblique solar illumination angles, indicating that the illumination geometry calculated from the DEM is wrong. The low reflectance values in the lower right corner of the scatter plot tell a similar but more ambiguous story. These dark pixels are well illuminated; they could represent a dark surface, or they might not truly be well illuminated.

Throughout the image, we may want to retrieve properties of the land surface by analyzing the reflectance. To do so we would use the topographic information and the *apparent* reflectance measured by the satellite sensor to estimate the *intrinsic* reflectance that the geophysical and biological properties govern. For some pixels, however, those retrievals of the surface properties would be wrong. This study characterizes the illumination errors in the globally available digital elevation models and recommends steps to mitigate these uncertainties in retrieval of Earth's properties in mountainous terrain.

3 Data and Methods

3.1 Acronyms

ASO	Airborne Snow Observatories.
ASTER	Advanced Spaceborne Thermal Emission and Reflection Radiometer.
AVIRIS-NG	Airborne Visible and Infrared Imaging Spectrometer – Next Generation.
CHIME	Copernicus Hyperspectral Imaging Mission for the Environment.
DEM	Digital elevation model of the bare Earth surface.
DSM	Digital surface model including vegetation, buildings, etc.
DTM	Same as DEM.
EROS	Earth Resources Observation and Science.
HMA	High Mountain Asia
IFSAR	Interferometric synthetic aperture radar.
InSAR	Same as IFSAR.
ISRO	Indian Space Research Organization.
NASA	National Aeronautics and Space Administration.
NOAA	National Oceanic and Atmospheric Administration.
OLI	Operational Land Imager.
SBG	Surface Biology and Geology mission.
SRTM	Shuttle Radar Topography Mission.
USGS	U.S. Geological Survey.
UTC	Coordinated Universal Time.

Ellipsoids and Geoids

EGM2008	Earth Gravitational Model 2008.
EGM96	Earth Gravitational Model 1996.
GRS80	Geodetic Reference System 1980.
NAD83	North American Datum of 1983.
NAVD88	North American Vertical Datum of 1988.
WGS84	World Geodetic System 1984.

3.2 Elevation data

We consider two resolutions of digital elevation models: fine and coarse. Table 1 summarizes the information sources for three fine-resolution and two global coarse-resolution datasets. For the fine-resolution imagery, our data are derived from three different methods: lidar altimetry, interferometric synthetic aperture radar, and structure-from-motion using fine-resolution commercial satellite imagery.

1. Airborne Snow Observatories Inc. (Painter et al., 2016) maps snow depth with lidar altimetry over drainage basins in the Western U.S., Switzerland, and Norway. The company acquires elevation data during the snow-free summer and then periodically measures the snow-on elevation during the winter and derives snow depth by subtraction. The company provided a 3 m DEM of the Carson River Watershed in the Sierra Nevada of California/Nevada, covering 2052 km^2.
2. The U.S. Geological Survey's Alaska Mapping Initiative acquired airborne InSAR data over much of Alaska in 2010 and 2012 (USGS EROS Archive, 2018). InSAR acquisitions can take place even in cloudy weather, and the data from a high latitude provide a broad range of solar illumination angles during the year. We downloaded and spliced tiles at 5 m resolution for a 2582 km^2 area in the Wrangell Mountains in Southeast Alaska.
3. Shean et al. (2016) employ structure-from-motion to measure elevation using commercial fine-resolution satellite imagery. From the National Snow and Ice Data Center, we downloaded part of the High Mountain Asia 8 m DEM for a 3514 km^2 area in the Himachal Pradesh state in the Indian Himalaya that covers 16 flight lines of the 2016 NASA-ISRO AVIRIS-NG campaign (Space Applications Centre, 2017).

Table 1. Information sources for digital elevation models used in the analysis.

Dataset	Datum Horizontal	Datum Vertical	Elevation Source	Projection	Spatial resolution
Fine resolution					
ASO DEM	WGS84	WGS84	airborne lidar	UTM Zone 11N	3 m
Alaska IFSAR DEM	NAD83	NAVD88	interferometric SAR	Alaska Albers*	5 m
HMA DEM	WGS84	WGS84	structure-from-motion	HMA Albers*	8 m
Coarse resolution					
Copernicus DEM	WGS84	EGM2008	TanDEM-X	geographic	1 arcsec
NASADEM	WGS84	EGM96	SRTM + ASTER	geographic	1 arcsec

*Albers equaconic projection.
Alaska origin 50°N, 154°W, standard parallels 55°N, 65°N.
HMA origin 36°N, 85°E, standard parallels 25°N, 47°N.

For the coarse resolution imagery, we used two global data sources at one arcsecond resolution distributed in geographic (latitude-longitude) format. In cropping to the boundaries of each fine-resolution area, we added 5 km to each edge to minimize edge effects in calculating topographic parameters.

1. We spliced 1° × 1° tiles from the NASADEM (Buckley, 2020) together because both areas of interest crossed latitude or longitude tile boundaries. The NASADEM combines information from the Shuttle Radar Topography Mission (Farr et al., 2007) and stereo-photogrammetry from ASTER imagery (NASA & METI, 2019).
2. We downloaded Copernicus DEMs (European Space Agency, 2021) that were spliced and distributed by Open Topography. The Copernicus DEM is derived from TanDEM-X imagery.

Figure 2 shows the Copernicus DEM and the ASO DEM for the Carson River Watershed. The small portion of the ASO DEM shown illustrates the detail of the topographic data at 3 m spatial resolution.

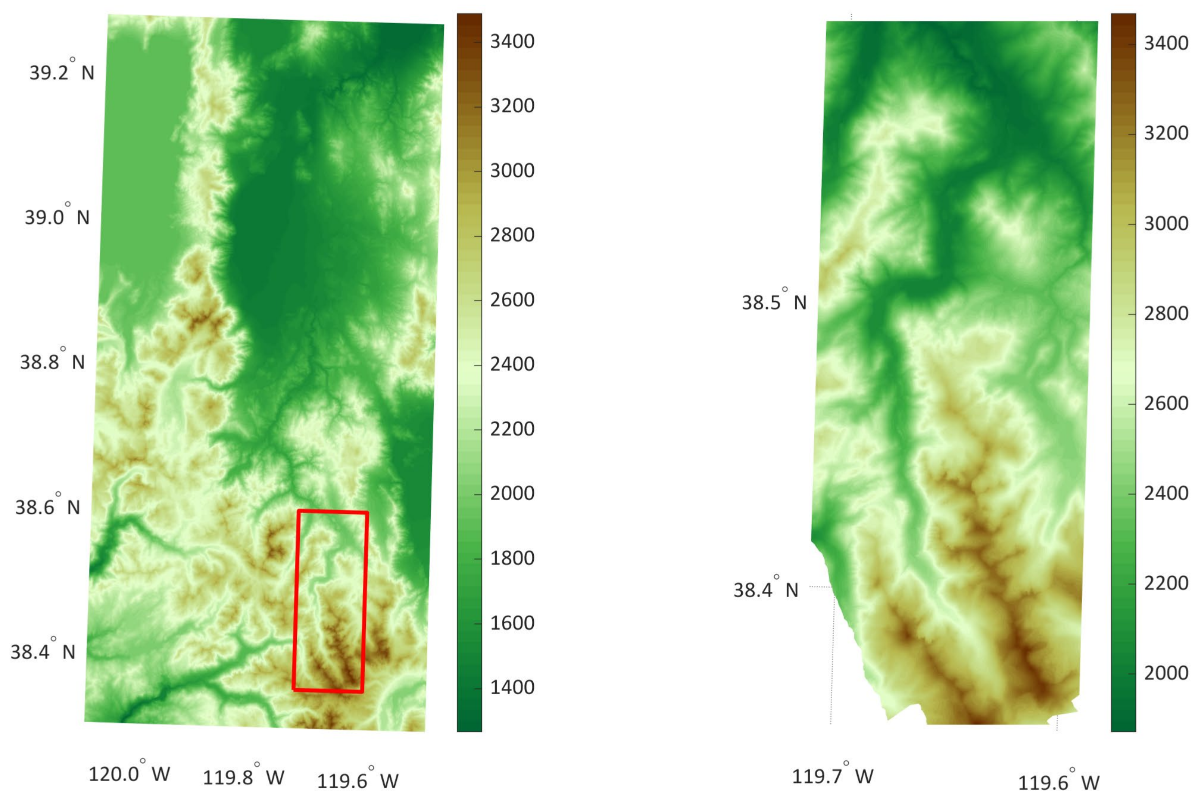

Figure 2. Example of the elevation sources for the Carson River Watershed. The left image shows the Copernicus DEM, whose spatial resolution is 1 arcsecond; the right image shows a segment of the ASO 3m DEM, showing detail. Both images are in a UTM projection, Zone 11N.

3.3 Notation

We selected or calculated the following variables for each grid point in each elevation dataset. θ_0, ϕ_0, and μ_S vary with date; the other variables are independent of date and thus the solar illumination. Deep snow can smooth the topography, but our comparisons of snow-off with snow-on elevations find only a few grid cells with significantly different slope and azimuth.

θ_0, ϕ_0	Solar zenith and azimuth angles, $\mu_0 = \cos\theta_0$.
μ_S	Cosine of illumination angle on a slope.
ρ	Spectral directional-hemispherical or bihemispherical reflectance, depending on subscripts (Schaepman-Strub et al., 2006).
F_{dif}	Fraction of incoming spectral irradiance that is diffuse.
$H(\phi)$	Horizon angle, upward from horizontal, in azimuth ϕ.
I	Spectral irradiance, incoming or reflected depending on subscript.
RMS	Root-mean-square value $RMS(x) = \sqrt{\frac{1}{N}\sum_{n=1}^{N}\lvert x_n\rvert^2}$.
S, A	Slope angle, upward from horizontal, and slope azimuth, south at 0°, eastward positive and westward negative, consistent with a right-hand coordinate system.
V_Ω	Sky view factor, the fraction of the upward hemisphere open to sky.
Z	Elevation of the surface.

3.4 Methods

We compared the variables by reprojecting both fine- and coarse-resolution data to an intermediate resolution approximating the geometric mean of the two resolutions, thereby to include the range and distribution of topographic values in the landscape. The one-arcsecond resolution of the NASADEM and Copernicus DEM translate to about 30 m. For the Carson River Watershed, the intermediate resolution between the 3 m ASO lidar and the globally available data is 10 m. For the InSAR data at 5 m over the Wrangell Mountains in Alaska, the intermediate resolution is 12 m. For the 8 m data in the HMA DEM, the intermediate resolution is 15 m. We assume the fine DEM is more accurate, particularly when variables derived over multiple points are compared to those derived from the coarse DEM; therefore, the RMS of the difference between the coarse and fine estimates of a variable is considered the RMS error.

We calculated μ_S for seven dates between the winter and summer solstices, spaced so that the intervals between the solar declinations were equal (Figure 3). For every date, we chose 10:45 in the local time zone, Pacific Standard (UTC–8:00) for the Carson River, Alaska Standard (UTC–9:00) for the Wrangell Mountains, and India Standard (UTC+5:30) for the Himachal Pradesh. Figure 4 shows cosine illumination values for the Himachal Pradesh on the seven dates in Figure 3.

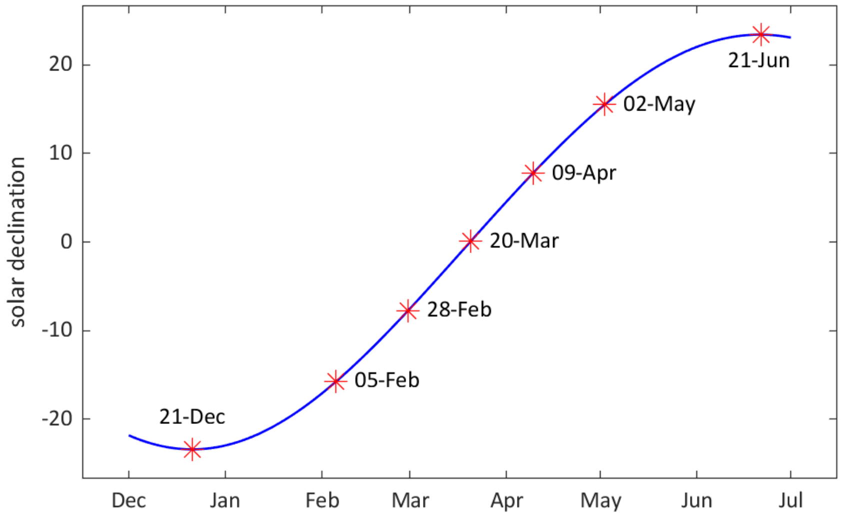

Figure 3. Dates and their solar declinations used in the analysis, spaced in equal latitude intervals from the winter solstice to the summer solstice (NOAA, n.d., solar calculator).

4 Results

Tables 2 and 3 summarize results for all fine- and coarse-resolution datasets analyzed. Figures 2 and 4 through 6 illustrate examples of the results, comparing one pair of variables derived from a fine- and a coarse-resolution image. We include examples from each of the three study sites: Carson River Watershed, Wrangell Mountains, and Indian Himalaya.

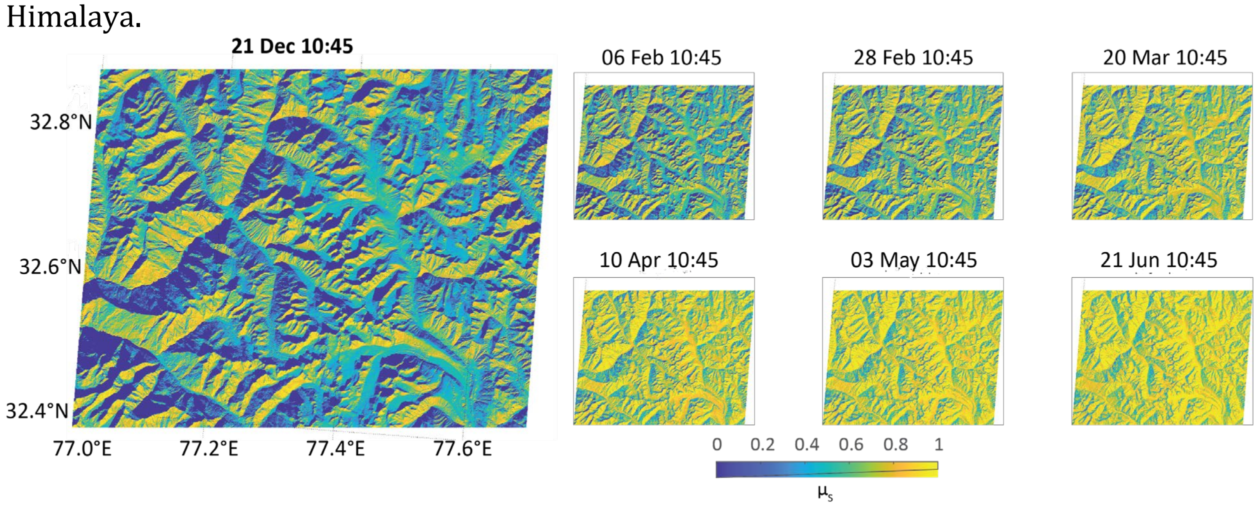

Figure 4. Values of μ_S (cosine of local illumination angle, including shadowing by horizons) over the Indian Himalaya at 10:45 am on the dates shown in Figure 3, from the winter to the summer solstice. The area coincides with 16 flight lines by AVIRIS-NG during the 2016 ISRO-NASA campaign. The illumination values are calculated from the High Mountain Asia 8 m DEM, which are in the HMA Albers Projection; parameters are Albers equaconic, origin 36°N 85°E, standard parallels 25°N and 47°N.

4.1 Topographic variables independent of solar illumination

Variations in elevation across topography translate to slopes and aspects, which combine with the solar illumination geometry to create variability in local illumination. The view factor controls the re-reflection of solar radiation that strikes the surface and the fraction of the diffuse irradiance and atmospheric thermal infrared irradiance that reaches the surface. For these reasons, the errors in elevation itself are less important than errors in the other topographic variables. Based on the differences between the fine-resolution and coarse-resolution DEMs, Table 2 shows the RMS error for elevation, slope, aspect, and view factor, along with "southness" and "eastness" variables to combine effects of slope and aspect. Because the differences between the datum sources (Table 1) for elevation exceed 25 m and because we are mostly interested in the internal differences in an elevation grid, we subtract the mean elevation of each grid from that grid's values before calculating the RMS errors for elevation. Errors in elevation are small fractions of the elevation values themselves, but the errors in slope and aspect indicate significant differences between elevations of neighboring points. Results for the NASADEM and the Copernicus DEM are similar, but both show outliers that translate into outliers in calculating illumination angles.

Table 2. Root-mean-square error statistics for topographic variables that are independent of solar illumination.

Dataset	Root-mean-square error: Elevation (m)	Slope (°)	Azimuth (°)	View factor	South-ness	East-ness
Copernicus DEM, Carson River	4.87	4.73	72.6	0.027	0.092	0.093
NASADEM, Carson River	6.51	6.24	75.2	0.034	0.115	0.118
Copernicus DEM, Wrangell Mountains	9.11	4.15	24.5	0.025	0.076	0.079
Copernicus DEM, Himachal Pradesh	15.66	6.42	26.3	0.039	0.123	0.129
NASADEM, Himachal Pradesh	12.06	6.60	26.7	0.040	0.127	0.132

$Southness = \sin S \cos A$. $Eastness = \sin S \sin A$.

Aspect values and their RMS errors must be treated with caution, because aspect has negligible effect on solar radiation when the slope is small but a huge effect when the slope is steep. To consider the interaction of slope and aspect, we also compute $Southness = \sin S \cos A$ and $Eastness = \sin S \sin A$. In our formulation, we follow the right-hand convention that 0° aspect represents south, from which eastward aspects are positive and westward aspects are negative (Sellers, 1965). Therefore, $Southness = 1$ represents a vertical south-facing slope.

The variability in the data indicate variation within the topographic grid. Figure 5 shows the scatter diagrams for the row in Table 2 that summarizes the statistics for the Copernicus DEM for the Carson River Watershed in the Sierra Nevada. In the more rugged terrains in the Wrangell Mountains and Indian Himalaya, the RMS error varies from 5 to 16 m. For elevation, the spread around the regression in Figure 5 is small. For the other variables, however, the spread is much larger. The prevalence of outliers in the scatter plots for slope and aspect suggests that outliers would be present in the local illumination angles. Slopes less than 20° in the ASO 3 m DEM correspond to slopes greater than 40° in the Copernicus 1 arcsecond DEM, and conversely slopes greater than 50° in the finer-resolution DEM correspond to slopes less than 20° in the Copernicus DEM. Similar differences occur in the aspects, view factors, and directional variables. In all cases, except elevation, the slopes of the regression lines that characterize the relationship between the coarse- and fine-resolution variables are less than 1.0, indicating generally that the Copernicus DEM and NASADEM slightly underestimate the magnitudes.

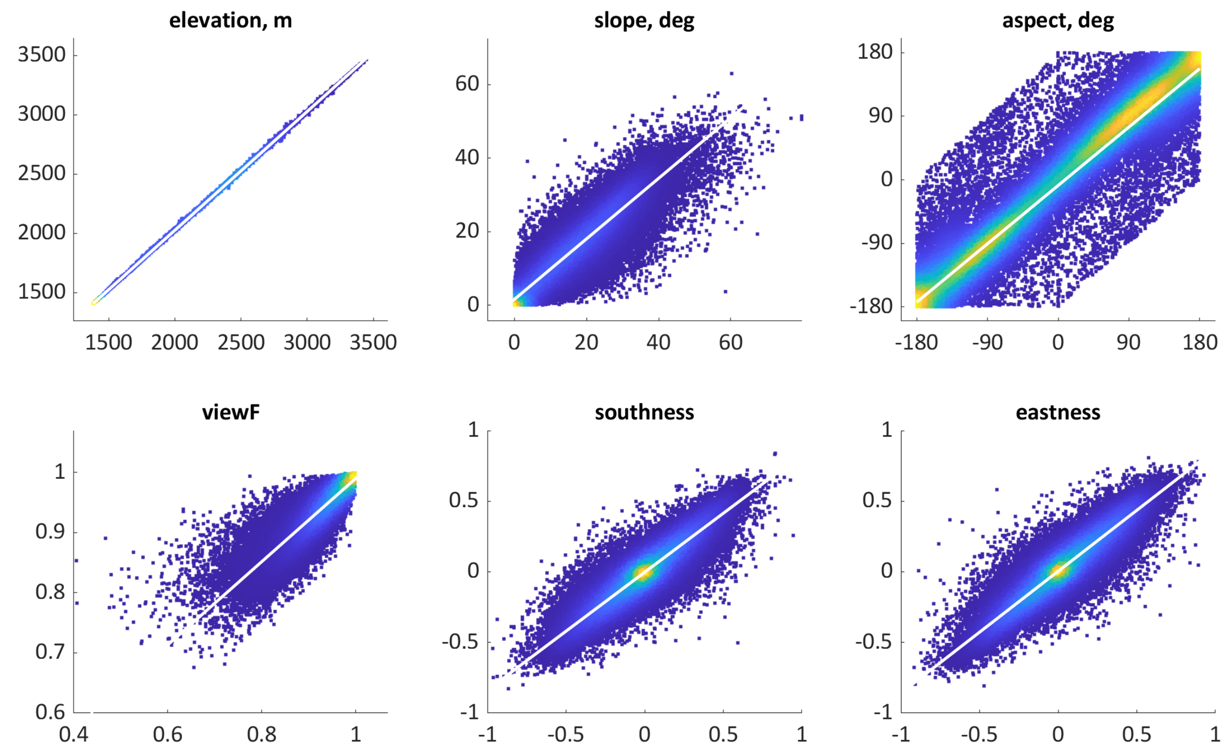

Figure 5. Detailed illustration supporting one row in Table 2, for the Copernicus DEM in the Carson River Watershed in the Sierra Nevada. The *x*-axes show data for the ASO 3 m DEM; the *y*-axes show the same information derived from the Copernicus DEM, with both DEMs reprojected to a common size and projection. Aspect angles represent south as 0°, eastward positive, westward negative, and therefore consistent with a right-hand coordinate system. Regression lines in the figure and statistics in Table 2 are based on the whole topographic grid, but just 100,000 points are randomly selected for the illustrative scatter plots. Regressions slopes are: elevation 1.00, slope 0.82, aspect 0.92, view factor 0.60, southness 0.83, eastness 0.86. Owing to the size of the dataset, the uncertainties in the calculated regression slopes are of order 10^{-4}.

4.2 Effect of topography on illumination and reflection

The two crucial topographic variables in order of importance are μ_S, the cosine of the local illumination angle measured from normal to the slope, and V_Ω, the fraction of the hemisphere over a point that is open to the sky. Over a flat unobstructed surface, $V_\Omega = 1$. The local illumination angle is related to the topography and the solar illumination geometry as:

$$\mu_S = \max[0, \mu_0 \cos S + \sin\theta_0 \sin S \cos(\phi_0 - A)] \tag{1}$$

The max function accounts for slopes facing away from the sun by setting $\mu_S = 0$ in situations where the equation would yield $\mu_S < 0$. To account for points where neighboring horizons block the Sun, we also set $\mu_S = 0$ where $\sin H(\phi_0) \geq \mu_0$. Dozier (2022a) presents the methods for rapid calculation of the horizon angle $H(\phi)$ for any azimuth ϕ and for estimating the view factor V_Ω as an integral of a function of $H(\phi)$ around the whole circle.

The variables μ_S and V_Ω affect the relationship between the *apparent* reflectance of the surface and its *intrinsic* reflectance that would be measured independent of any topographic effects (Bair et al., 2022). The apparent reflectance of a topographic surface involves multiple reflections, especially for bright surfaces such as snow. Let ρ indicate spectral reflectance, omitting a wavelength identifier, and F_{dif} as the fraction of the spectral irradiance that is diffuse. Set the initial irradiance on a horizontal surface to *I*. The spectral radiation that initially escapes into the overlying hemisphere without being re-reflected is:

$$I_{esc}^{(0)} = IV_\Omega \left[\frac{\mu_S}{\mu_0}(1 - F_{dif})\rho_{intrinsic}^{(direct)} + F_{dif}\rho_{intrinsic}^{(diffuse)} + (1 - V_\Omega)\left(\rho_{intrinsic}^{(diffuse)}\right)^2\right] \quad (2)$$

The superscripts designate the reflectance to direct vs. diffuse irradiance. The right-most term inside the brackets accounts for reflected radiation within a point's field-of-view impinging on the point. The direct and diffuse spectral albedos might differ slightly, for example for snow.

Not all the initially reflected radiation escapes into the overlying hemisphere. Instead, some of it re-reflects and eventually escapes or is trapped by the roughness, in which case it is subject to internal reflection. At the first iteration, its value is:

$$I_{internal}^{(0)} = I_{esc}^{(0)}\left(\frac{1 - V_\Omega}{V_\Omega}\right). \quad (3)$$

To account for multiple reflections, at each reflection the value of the incident radiation is multiplied by the fraction $(1 - V_\Omega)$ that accounts for the reflection remaining within the topography, the fraction V_Ω that escapes, and the spectral reflectance. An orders-of-scattering approach to the multiple reflections lets some reflected radiation escape at each iteration *n* and some remains available for re-reflection:

$$\begin{aligned} \text{escaped } I_{esc}^{(n)} &= I_{internal}^{(n-1)}\rho_{intrinsic}^{(diffuse)}V_\Omega \\ \text{remaining } I_{internal}^{(n)} &= I_{internal}^{(n-1)}\rho_{intrinsic}^{(diffuse)}(1 - V_\Omega) \end{aligned} \quad (4)$$

This series converges in a half dozen iterations because $I_{internal}^{(n)}$ declines in proportion to $(1 - V_\Omega)^n$. The apparent reflectance for the pixel is $\rho_{apparent} = \sum I_{esc}/I$.

4.3 Errors in estimating μ_S, the cosine of local illumination

RMS errors and outliers in the topographic variables combine with the solar illumination geometry to propagate into the calculation of each pixel's illumination. The most important variable whose accuracy affects the interpretation of the remotely sensed signal is the cosine of the location illumination angle. The ratio μ_S/μ_0 appears in Equation (2), but μ_0 is usually known accurately. The view factor V_Ω affects the diffuse irradiance from the sky and the internal reflections within the topography.

Therefore, the accuracy of the cosine of illumination from the DEM affects our ability to calculate or correct for the topographic effects. For example, attempting to invert Equation (2) would use the ratio μ_0/μ_S; uncertainty in the denominator of a fraction often has significant consequences, especially if the denominator is small (Richter & Schläpfer, 2021, chapter 7). Table 3 shows the RMS errors for the cosine of illumination, along with the fraction of the terrain that is shadowed, for the dates in Figure 3 that extend from the winter to the summer solstice in equal changes of the solar declination. The RMS error for μ_S varies inversely with the value of μ_0; the errors in slope S and aspect A (Table 2) have a greater effect when μ_0 is smaller.

Table 3. Shadowed fraction and RMS error of μ_S (cosine illumination) for each date in each dataset, varying monotonically with the solar zenith angle $\mu_0 = \cos\theta_0$. In each case the "fine" DEM is that cited for that region.

The full extent of errors in the results indicates issues with outliers that the RMS errors do not reveal. Figure 6 shows scatter diagrams of μ_s calculated from the Copernicus DEM vs μ_s calculated from the Alaska IFSAR DEM. On all dates but particularly early in the year, some pixels that are illuminated ($\mu_S \gg 0$) in the Copernicus DEM are dark ($\mu_S < 0.1$) in the Alaska IFSAR DEM. Similarly, some pixels that the Alaska IFSAR DEM shows to be illuminated are dark in the Copernicus DEM. A popular text on surveying published six decades ago (Davis et al., 1966) calls these kinds of mistakes "blunders" rather than errors, because they cannot be characterized by an error distribution.

5 Discussion

Although errors in the NASADEM and Copernicus DEM are small compared to the elevation values, their impact on remote sensing can be large. To the extent that errors of neighboring points are independent, the variances of the differences in elevations are the sum of the variances in the elevations themselves. Thus, the small dispersion around the 1:1 line in the scatter diagram for elevation in Figure 5 translates to much greater dispersion in the slope, aspect, and view factor, which in turn translate to large dispersion in the illumination angles that Figure 6 shows. Therefore, small errors in slope or aspect can then have a significant impact on estimated reflectance, especially wherever μ_S is small.

Algorithms differ in their sensitivities to topographic uncertainty. The effect is mostly a shift in radiance magnitude, so algorithms that rely on relative spectral shapes may escape significant harm. These include detection of materials based on diagnostic spectral absorptions, as in mineral identification (Clark et al., 2003). On the other hand, studies that rely on absolute radiometry, such as surface energy balance investigations (Wang et al., 2015), could be more severely affected. Moreover, errors in μ_S change the balance between diffuse and direct illumination onto the surface. Therefore, they can distort the estimated reflectance spectrum in visible wavelengths, harming snow or vegetation studies that rely on features in this spectral range.

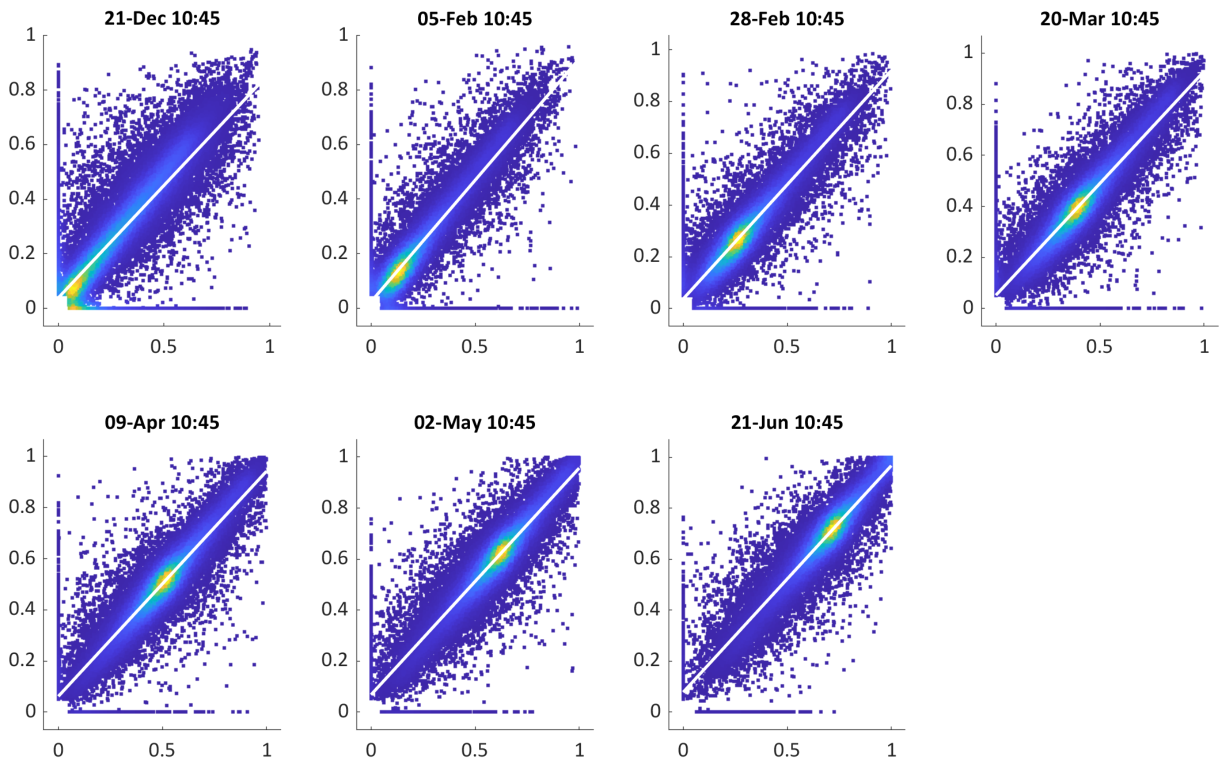

Figure 6. Detailed illustration supporting one row in Table 3, for the Copernicus DEM in the Wrangell Mountains. All axes show values of μ_S, the cosine of local illumination. The *x*-axes show values of calculated from the Alaska IFSAR DEM at 5 m resolution; the *y*-axes show the same values computed from the Copernicus DEM at 1 arcsecond, both reprojected to a common size and projection. Points along either the x- or y-axis identify locations that are shadowed in one DEM and illuminated in the other. Regression lines in the figure and statistics in Table 3 are based on all pixels in the data, but just 100,000 points are randomly selected for the illustrative scatter density plots. Note that the yellow values in the scatter density plots migrate to higher values of μ_S as the solar declination moves northward.

Illumination geometry in mountains affects current satellite imagery from Landsat 8/9 and Sentinel-2a/b, and it will affect future imagery from imaging spectrometers EnMAP, EMIT, SBG, and CHIME. Locally, fine-resolution DEMs will be available from lidar, InSAR, or structure-from-motion deployed from drones or aircraft, and slightly coarser DEMs will be available using structure-from-motion from spaceborne data. However, the prospect is unlikely for globally available data to accurately estimate the illumination geometry for these imaging satellites. A chapter in *Thriving on our Changing Planet* (National Academies of Science, Engineering, & Medicine, 2018, p. 513) identifies applications that "would benefit from multibeam, space-based lidar to obtain global coverage of bare-earth topography and of the biomass/canopy at <<5 m spatial and 0.1 m vertical resolutions." However, no such recommendation carried through to that report's Executive Summary, and no future NASA mission is in the planning stages.

Therefore, we face a future where the globally available DEMs are what we have now, at least through the launches and initial few years of the spectrometers SBG and CHIME and future versions of Landsat and Sentinel. If we could trust the variables calculated from DEMs and consider only the RMS errors, we could implement topographic correction algorithms that estimate $\rho_{intrinsic}$ from measurements of $\rho_{apparent}$ and thereby recover the geophysical and biological properties of the surface that govern spectral reflectance, with known uncertainty. However, we face the problem of outliers in the calculations of μ_S and less crucially V_Ω, so applying any correction algorithm globally on entire images would produce some incorrect, thus misleading, interpretations.

Strategies to mitigate the impact of topographic errors in processing and distributing image data and products must be considered. The list is deliberately terse; any bullet point could be expanded to a whole journal article:

- In the basis documents for algorithms for geophysical and biological products, assess their sensitivity to uncertainty in illumination geometry and distinguish between topographic effects that change the spectral shape of the signal vs. those that change the magnitude only (Lamare et al., 2020).
- Gain a better understanding of the use of shade endmembers (Adams et al., 1986) in spectral mixture analysis, which implicitly acknowledge the limitations of available DEMs.
- Understand the relative magnitudes of topographic effects on angular properties of the reflectance vs. the effects of illumination and viewing geometry on the intrinsic reflectance (Roupioz et al., 2014; Schaepman-Strub et al., 2006).
- Consider and validate methods to process images that identify pixels where the illumination geometry calculated from the matching DEM is clearly wrong, for example detection of shadowed terrain (Hollstein et al., 2016; Shahtahmassebi et al., 2013).
- Avoid exclusively prescribing global topographic correction solutions. Preserve the flexibility, within the mission science data system, for investigators to apply new regional DEMs of higher accuracy as these become available, or to ignore topography.

In the longer term, future research may reduce DEM-induced reflectance errors through strategies such as the following:

- Implement topographic corrections in superpixels, thereby smoothing out the errors in individual pixels (Gilmore et al., 2011).
- Continue efforts to improve DEMs globally, especially in mountainous areas (for example the USGS 3D elevation program in the U.S., Stoker & Miller, 2022).
- Examine and validate novel methods to estimate the illumination geometry directly from hyperspectral images.

6 Conclusions

Our analyses show that calculations in the globally available DEMs miss shadows and consistently underestimate the cosines of illumination angles—its RMS error increasing with solar zenith angle. Analyzing imagery of Earth's mountains from current and future missions requires addressing the uncertainty introduced by errors and outliers in the DEMs on algorithms that retrieve surface properties from measurements of the apparent spectral reflectance. Intriguing potential improvements lie in assessing the uncertainties in retrievals of geophysical and biological properties and in novel methods to gain information about topography from the imagery itself.

Acknowledgments

All authors declare no real or perceived financial conflicts of interests. A portion of this work was carried out at the Jet Propulsion Laboratory, California Institute of Technology, under NASA Award 80NM0018D0004. Amazon Web Services (AWS) Cloud Credit for Research Program provided computing support. The following authors acknowledge specific support: JD, NASA Award 80NSSC21K0620; EHB, NASA Awards 80NSSC21K0997, 80NSSC20K1722, 80NSSC20K1349, and 80NSSC18K1489; THP, NASA Award 80NSSC19K0645:P00003.

Open Research

We have assembled all elevation data used in this research in Dryad (Dozier, 2022b). Those files include splicing and cropping to match areas of fine and coarse resolution.

Public sources of the data are:

- NASADEM tiles are available from the U.S. Geological Survey Land Processes DAAC Data Pool (NASA JPL, 2020). Registration is required but is free.
- Copernicus DEMs customized to specific latitude-longitude quadrilaterals are available from Open Topography (European Space Agency, 2021).
- Airborne Snow Observatories Inc. provided the snow-off elevation data at 3 m spatial resolution for the Carson River Watershed.
- The Alaska elevation data, acquired by airborne interferometric synthetic aperture radar, are available from the U.S. Geological Survey (USGS EROS Archive, 2018).
- Tiles for the High Mountain Asia 8 m DEM are available at the National Snow and Ice Data Center (Shean, 2017).
- Global grids of the EGM96 and EGM2008 Geoids are available from Agisoft (2008).

Computer codes for calculating solar illumination geometry (Dozier, 2020) and topographic horizons and other terrain parameters (Dozier, 2022c) are available from the MATLAB Central file exchange. Code for reprojecting raster data is on GitHub (Dozier, 2021).

References

Adams, J. B., Smith, M. O., & Johnson, P. E. (1986). Spectral mixture modeling: A new analysis of rock and soil types at the Viking Lander 1 Site. *Journal of Geophysical Research: Solid Earth, 91*, 8098-8112. https://doi.org/10.1029/JB091iB08p08098

Agisoft. (2008). *Global Geoid Models* [Datasets]. https://www.agisoft.com/downloads/geoids/

Bair, E. H., Stillinger, T., & Dozier, J. (2021). Snow Property Inversion from Remote Sensing (SPIReS): A generalized multispectral unmixing approach with examples from MODIS and Landsat 8 OLI. *IEEE Transactions on Geoscience and Remote Sensing, 59*, 7270-7284. https://doi.org/10.1109/TGRS.2020.3040328

Bair, E. H., Dozier, J., Stern, C., LeWinter, A., Rittger, K., Savagian, A., Stillinger, T., & Davis, R. E. (2022). Divergence of apparent and intrinsic snow albedo over a season at a sub-alpine site with implications for remote sensing. *The Cryosphere, 16*, 1765-1778. https://doi.org/10.5194/tc-16-1765-2022

Barros, A. P. (2013). Orographic precipitation, freshwater resources, and climate vulnerabilities in mountainous regions. In R. Pielke (Ed.), *Climate Vulnerability: Understanding and Addressing Threats to Essential Resources* (pp. 57-78). Oxford: Academic Press. https://doi.org/10.1016/B978-0-12-384703-4.00504-9

Bogan, S. A., Antonarakis, A. S., & Moorcroft, P. R. (2019). Imaging spectrometry-derived estimates of regional ecosystem composition for the Sierra Nevada, California. *Remote Sensing of Environment, 228*, 14-30. https://doi.org/10.1016/j.rse.2019.03.031

Buckley, S. (2020). NASADEM: Creating a new NASA digital elevation model and associated products. NASA. https://earthdata.nasa.gov/esds/competitive-programs/measures/nasadem

Clark, R. N., Swayze, G. A., Livo, K. E., Kokaly, R. F., Sutley, S. J., Dalton, J. B., McDougal, R. R., & Gent, C. A. (2003). Imaging spectroscopy: Earth and planetary remote sensing with the USGS Tetracorder and expert systems. *Journal of Geophysical Research: Planets, 108*, 5131. https://doi.org/10.1029/2002JE001847

Davis, R. E., Foote, F. S., & Kelly, J. W. (1966). *Surveying Theory and Practice* (5th ed.). New York: McGraw-Hill.

Dozier, J. (2020). Sun position: functions for declination, solar longitude, radius vector, equation of time, times of sunrise and sunset, sun angles and azimuths. Natick, MA: MATLAB Central File Exchange. https://www.mathworks.com/matlabcentral/fileexchange/74939-sun-position.

Dozier, J. (2021). Raster reprojection. https://github.com/DozierJeff/RasterReprojection.

Dozier, J. (2022a). Revisiting topographic horizons in the era of big data and parallel computing. *IEEE Geoscience and Remote Sensing Letters, 19*, 8024605. https://doi.org/10.1109/LGRS.2021.3125278

Dozier, J. (2022b). *Topographic data to support the analysis of error and uncertainty that degrade topographic corrections of remotely sensed data* [Dataset distributed by Dryad]. https://doi.org/10.25349/D9B62G

Dozier, J. (2022c). Topographic horizons: angles to the horizons from an elevation grid with options for parallelism (Version 4.4). Natick, MA: MATLAB Central File Exchange. https://www.mathworks.com/matlabcentral/fileexchange/94800-topographic-horizons.

European Space Agency. (2021). *Copernicus Global Digital Elevation Model* [Distributed by Open Topography]. https://doi.org/10.5069/G9028PQB

Farr, T. G., Rosen, P. A., Caro, E., Crippen, R., Duren, R., Hensley, S., Kobrick, M., Paller, M., Rodriguez, E., Roth, L., Seal, D., Shaffer, S., Shimada, J., Umland, J., Werner, M., Oskin, M., Burbank, D., & Alsdorf, D. (2007). The Shuttle Radar Topography Mission. *Reviews of Geophysics, 45*, RG2004. https://doi.org/10.1029/2005RG000183

Gilmore, M. S., Thompson, D. R., Anderson, L. J., Karamzadeh, N., Mandrake, L., & Castaño, R. (2011). Superpixel segmentation for analysis of hyperspectral data sets, with application to Compact Reconnaissance Imaging Spectrometer for Mars data, Moon Mineralogy Mapper data, and Ariadnes Chaos, Mars. *Journal of Geophysical Research: Planets, 116*, E07001. https://doi.org/10.1029/2010JE003763

Guth, P. L., & Geoffroy, T. M. (2021). LiDAR point cloud and ICESat-2 evaluation of 1 second global digital elevation models: Copernicus wins. *Transactions in GIS, 25*, 2245-2261. https://doi.org/10.1111/tgis.12825

Hollstein, A., Segl, K., Guanter, L., Brell, M., & Enesco, M. (2016). Ready-to-use methods for the detection of clouds, cirrus, snow, shadow, water and clear sky pixels in Sentinel-2 MSI images. *Remote Sensing, 8*, 666. https://doi.org/10.3390/rs8080666

Immerzeel, W. W., Lutz, A. F., Andrade, M., Bahl, A., Biemans, H., Bolch, T., Hyde, S., Brumby, S., Davies, B. J., Elmore, A. C., Emmer, A., Feng, M., Fernández, A., Haritashya, U., Kargel, J. S., Koppes, M., Kraaijenbrink, P. D. A., Kulkarni, A. V., Mayewski, P. A., Nepal, S., Pacheco, P., Painter, T. H., Pellicciotti, F., Rajaram, H., Rupper, S., Sinisalo, A., Shrestha, A. B., Viviroli, D., Wada, Y., Xiao, C., Yao, T., & Baillie, J. E. M. (2020). Importance and vulnerability of the world's water towers. *Nature, 577*, 364-369. https://doi.org/10.1038/s41586-019-1822-y

Kirschbaum, D., Kapnick, S. B., Stanley, T., & Pascale, S. (2020). Changes in extreme precipitation and landslides over High Mountain Asia. *Geophysical Research Letters, 47*, e2019GL085347. https://doi.org/10.1029/2019GL085347

Lamare, M., Dumont, M., Picard, G., Larue, F., Tuzet, F., Delcourt, C., & Arnaud, L. (2020). Simulating optical top-of-atmosphere radiance satellite images over snow-covered rugged terrain. *The Cryosphere, 14*, 3995-4020. https://doi.org/10.5194/tc-14-3995-2020

Mankin, J. S., Viviroli, D., Singh, D., Hoekstra, A. Y., & Diffenbaugh, N. S. (2015). The potential for snow to supply human water demand in the present and future. *Environmental Research Letters, 10*, 114016. https://doi.org/10.1088/1748-9326/10/11/114016

Moody, J. A., & Martin, D. A. (2001). Post-fire, rainfall intensity–peak discharge relations for three mountainous watersheds in the western USA. *Hydrological Processes, 15*, 2981-2993. https://doi.org/10.1002/hyp.386

NASA & METI. (2019). *ASTGTM V003: ASTER Global Digital Elevation Model 1 arc second* [Distributed by USGS Land Processes DAAC]. https://doi.org/10.5067/ASTER/ASTGTM.003

NASA JPL. (2020). *NASADEM Merged DEM Global 1 arc second V001* [Dataset distributed by USGS Land Processes DAAC]. https://doi.org/10.5067/MEaSUREs/NASADEM/NASADEM_HGT.001

National Academies of Sciences, Engineering, & Medicine. (2018). *Thriving on Our Changing Planet: A Decadal Strategy for Earth Observation from Space*. Washington, DC: National Academies Press. https://doi.org/10.17226/24938

NOAA. (n.d.). NOAA solar calculator. Boulder, CO: NOAA Earth System Research Laboratory. http://www.esrl.noaa.gov/gmd/grad/solcalc/

Painter, T. H., Seidel, F. C., Bryant, A. C., Skiles, S. M., & Rittger, K. (2013). Imaging spectroscopy of albedo and radiative forcing by light-absorbing impurities in mountain snow. *Journal of Geophysical Research-Atmospheres, 118*, 9511-9523. https://doi.org/10.1002/jgrd.50520

Painter, T. H., Berisford, D. F., Boardman, J. W., Bormann, K. J., Deems, J. S., Gehrke, F., Hedrick, A., Joyce, M., Laidlaw, R., Marks, D., Mattmann, C., McGurk, B., Ramirez, P., Richardson, M., Skiles, S. M., Seidel, F. C., & Winstral, A. (2016). The Airborne Snow Observatory: Fusion of scanning lidar, imaging spectrometer, and physically-based modeling for mapping snow water equivalent and snow albedo. *Remote Sensing of Environment, 184*, 139-152. https://doi.org/10.1016/j.rse.2016.06.018

Richter, R., & Schläpfer, D. (2021). *ATCOR Theoretical Background*. CH-9500 Wil, Switzerland: ReSe Applications. https://www.rese-apps.com/pdf/atcor_atbd.pdf

Roupioz, L., Nerry, F., Jia, L., & Menenti, M. (2014). Improved surface reflectance from remote sensing data with sub-pixel topographic information. *Remote Sensing, 6*, 10356-10374. https://doi.org/10.3390/rs61110356

Schaepman-Strub, G., Schaepman, M. E., Painter, T. H., Dangel, S., & Martonchik, J. V. (2006). Reflectance quantities in optical remote sensing—definitions and case studies. *Remote Sensing of Environment, 103*, 27-42. https://doi.org/10.1016/j.rse.2006.03.002

Sellers, W. D. (1965). *Physical Climatology*. Chicago: University of Chicago Press.

Shahtahmassebi, A. R., Yang, N., Wang, K., Moore, N., & Shen, Z. (2013). Review of shadow detection and de-shadowing methods in remote sensing. *Chinese Geographical Science, 23*, 403-420. https://doi.org/10.1007/s11769-013-0613-x

Shean, D. E., Alexandrov, O., Moratto, Z. M., Smith, B. E., Joughin, I. R., Porter, C., & Morin, P. (2016). An automated, open-source pipeline for mass production of digital elevation models (DEMs) from very-high-resolution commercial stereo satellite imagery. *ISPRS Journal of Photogrammetry and Remote Sensing, 116*, 101-117. https://doi.org/10.1016/j.isprsjprs.2016.03.012

Shean, D. E. (2017). *High Mountain Asia 8-meter DEM mosaics derived from optical imagery, Version 1* [Distributed by National Snow and Ice Data Center]. https://doi.org/10.5067/KXOVQ9L172S2

Shugart, H. H., French, N. H. F., Kasischke, E. S., Slawski, J. J., Dull, C. W., Shuchman, R. A., & Mwangi, J. (2001). Detection of vegetation change using reconnaissance imagery. *Global Change Biology, 7*, 247-252. https://doi.org/10.1046/j.1365-2486.2001.00379.x

Space Applications Centre. (2017). *Spectrum of India*. Bangalore: Indian Space Research Organisation.

Stoker, J., & Miller, B. (2022). The accuracy and consistency of 3D elevation program data: a systematic analysis. *Remote Sensing, 14*, 940. https://doi.org/10.3390/rs14040940

USGS EROS Archive. (2018). *Digital Elevation - Interferometric Synthetic Aperture Radar (IFSAR) - Alaska* [Distributed by Earth Resources Observation and Science (EROS) Center]. https://doi.org/10.5066/P9C064CO

Uuemaa, E., Ahi, S., Montibeller, B., Muru, M., & Kmoch, A. (2020). Vertical accuracy of freely available global digital elevation models (ASTER, AW3D30, MERIT, TanDEM-X, SRTM, and NASADEM). *Remote Sensing, 12*, 3482. https://doi.org/10.3390/rs12213482

Viviroli, D., Dürr, H. H., Messerli, B., Meybeck, M., & Weingartner, R. (2007). Mountains of the world, water towers for humanity: Typology, mapping, and global significance. *Water Resources Research, 43*, W07447. https://doi.org/10.1029/2006WR005653

Wang, D., Liang, S., He, T., & Shi, Q. (2015). Estimating clear-sky all-wave net radiation from combined visible and shortwave infrared (VSWIR) and thermal infrared (TIR) remote sensing data. *Remote Sensing of Environment, 167*, 31-39. https://doi.org/10.1016/j.rse.2015.03.022